



HAL
open science

Inferring the rheology of the crust from the uplift observed above the Altiplano-Puna Magma Body

Nicolò R Sgreva, Anna Massmeyer, Anne Davaille

► **To cite this version:**

Nicolò R Sgreva, Anna Massmeyer, Anne Davaille. Inferring the rheology of the crust from the uplift observed above the Altiplano-Puna Magma Body. *Geophysical Journal International*, 2022, 10.1093/gji/ggac258 . hal-03518450

HAL Id: hal-03518450

<https://hal.science/hal-03518450>

Submitted on 9 Jan 2022

HAL is a multi-disciplinary open access archive for the deposit and dissemination of scientific research documents, whether they are published or not. The documents may come from teaching and research institutions in France or abroad, or from public or private research centers.

L'archive ouverte pluridisciplinaire **HAL**, est destinée au dépôt et à la diffusion de documents scientifiques de niveau recherche, publiés ou non, émanant des établissements d'enseignement et de recherche français ou étrangers, des laboratoires publics ou privés.

Inferring the rheology of the crust from the uplift observed above the Altiplano-Puna Magma Body

Nicolò R. Sgreva^{a,*}, Anna Massmeyer^b, Anne Davaille^c

^a*Université de Lorraine, CNRS, LEMTA, 54000, Nancy, France*

^b*Institute of Heat and Mass Transfer, RWTH Aachen University, Augustinerbach 6,
52056 Aachen, Germany*

^c*Université Paris-Saclay, CNRS, FAST, 91405, Orsay, France*

Abstract

Geophysical imaging techniques together with numerical models have shown that the surface uplift measured above the Altiplano-Puna Magma Body (APMB) can be resolved by the presence and propagation of a diapir from the top of the APMB itself. In this work we interpret deformations that characterize the crustal region above and around APMB through the employment of a viscoplastic type rheology. That is, we assume that at large scale the ductile lower-middle crust that surround the magmatic mush behaves as yield-stress fluid described by a Herschel-Bulkley (HB) model. In this scenario, the main critical conditions needed for the growth and the subsequent rise of the diapir are: (1) the ratio between yield stress and viscous stresses, namely the Bingham number Bi , has to be less than 1, i.e. $Bi \leq 1$; and (2) the ratio between buoyancy stresses and yield stress, namely the inverse of the Yield number $Y_{inv}=Y^{-1}$, has to be larger than a critical value, i.e. $Y_{inv} > Y_{invC}$. By using these critical conditions we infer the bulk

*nicolo.sgreva@univ-lorraine.fr

rheological properties of the heterogeneous lower-middle crust above APMB. We estimate the yield stress of the crust in between 0.5-15 MPa. For a crust that allows the development and the emerge of a 10 to 100 km wide diapir, the coupling of this range of yield stress with the regional uplift velocity measured at the surface allows to estimate a critical strain rate of $\sim 10^{-15}$ - 10^{-16} s⁻¹ and a maximum bulk effective viscosity of the lower-middle crust of $\eta_c=10^{21}$ Pa s.

Keywords: Rheology: crust and lithosphere, APMB, Diapirism, Yield stress, Viscoplastic

1. Introduction

The Altiplano-Puna Magma Body (APMB) is a mid-crustal magmatic system located at ~ 20 km beneath the Altiplano-Puna Volcanic Complex (APVC) in the central Andes, South America. It represents the largest active, continental magma body in Earth's crust (Zandt et al., 2003) and is considered to be directly related to an uplifting region, centered on the western slope of Uturuncu volcano, and its peripheral subsidence zone (Fig. 1) (Fialko and Pearse, 2012). The entire APMB can be represented as a complex transcrustal magmatic structure, that is a large environment volumetrically dominated by crystal mush (Cashman et al., 2017; Pritchard et al., 2018). Given its impact to the region, a good description of its dynamics becomes crucial to understand both its mobility, lifetime, internal structure (e.g. Massol and Jaupart, 2009; Gonnermann and Manga, 2007; Caricchi et al., 2007; Turner and Costa, 2007) and the role that such an enormous ($\sim 5 \times 10^5$ km³, Ward et al. (2014)) magmatic structure can play on the deformation of the

16 overlying crust.

17 However, to constrain the mush dynamics beneath APVC and the thermo-
18 mechanical response of the surrounding region, a number of geometrical and
19 physical properties of both APMB and lower-middle crust are required. Some
20 of them have been constrained in recent years by using different geophysical
21 investigation methods. For instance, by combining seismic tomography and
22 3D-model inversion to evaluate the crustal 3D shear-wave velocity field, Ward
23 et al. (2014) displayed a very large ($\sim 5 \times 10^5 \text{ km}^3$) low seismic velocity (LSV)
24 zone at a depth of 4-25 km beneath the APVC. This region is interpreted
25 as an hotter zone compared to the surrounding material, and may also be
26 enriched in melt content. A similar broad LSV zone centered below the
27 Uturuncu volcano and at ~ 15 km below sea level has been revealed also by
28 other authors (e.g. Zandt et al., 2003; Chmielowski et al., 1999). However,
29 due to the resolution of seismic tomography that is not better than 1 km
30 (Cashman et al., 2017), the exact geometry and position of this hot body are
31 still debated. This is caused by the difficulty in constraining the spacial melt
32 distribution with the technique, which is not always able to recognize large
33 melt bodies even in regions that are active nowadays or have produced large
34 eruptions in the Quaternary (Cashman et al., 2017).

35 Besides seismic tomography, other geophysical imaging techniques can
36 help to better characterize this anomalous structure. Magnetotelluric data
37 reveals a first large low electrical resistivity ($< 3 \text{ } \Omega\text{m}$) anomaly at ~ 15 km
38 below the sea level and a second ~ 10 -km-wide vertical anomaly on the top
39 of it (Fig. 1c) (Comeau et al., 2015, 2016). Differences in resistivity between
40 the two regions may be related to variations in the composition: while the

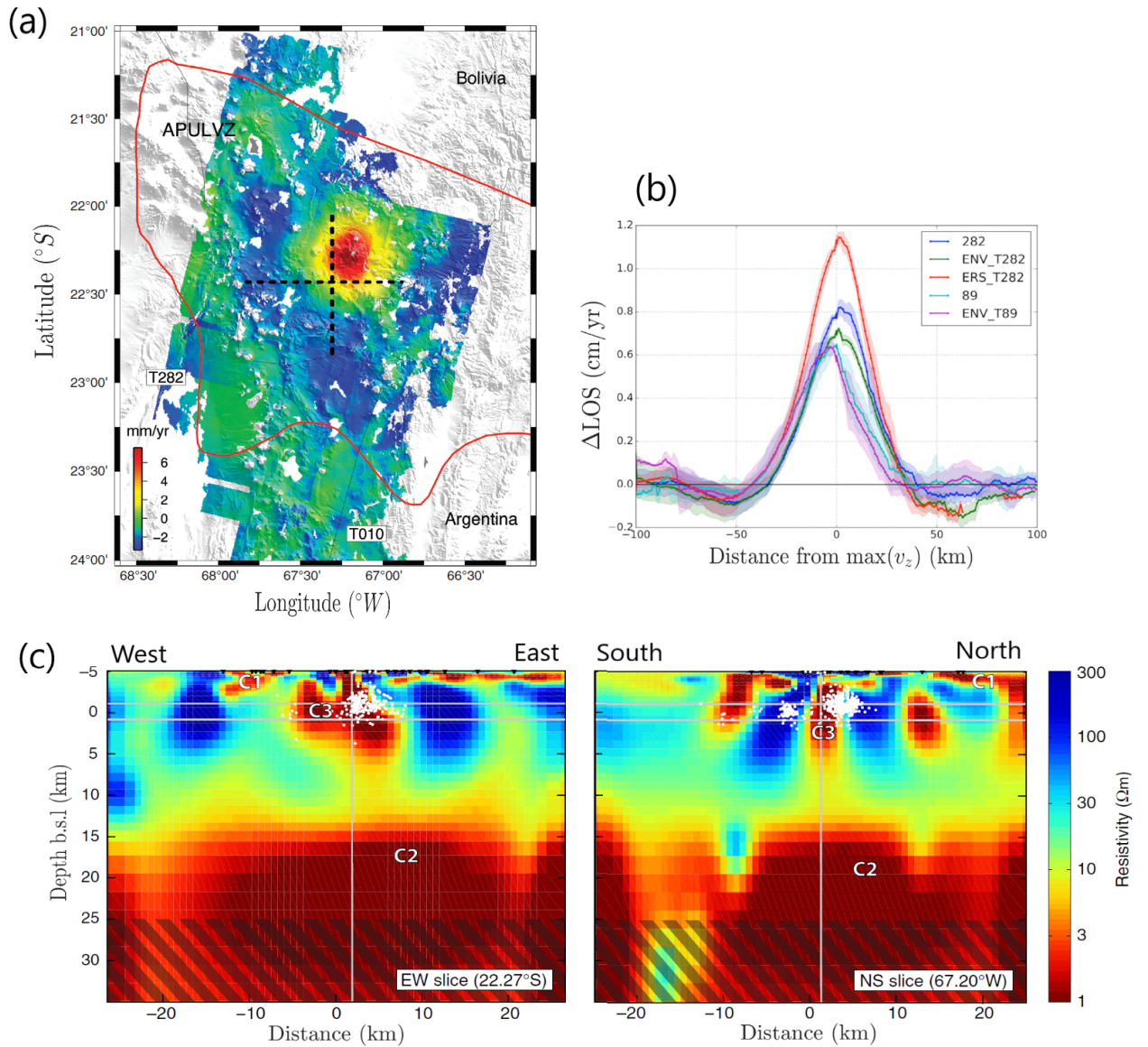


Figure 1: (a) Map view of the Altiplano-Puna region (Southern Bolivia). Colors indicate the elevation rate measured at the surface from InSAR data. Red line indicates the mid-crustal low-velocity zone associated to the APMB. Black dotted lines indicate the locations of cross sections in (c). Modified from Fialko and Pearce (2012). (b) Average velocities of line of sight (LOS) along sections crossing the center of the uplift. Modified from Gottsmann et al. (2017). (c) West-East and South-North vertical cross sections of the 3D resistivity model of (Comeau et al., 2015) across APVC. The main low electrical resistivity anomaly (C2) is associated to the APMB whereas the smaller anomaly on the top of it (C3) is interpreted as an ascent diapir. Modified from Comeau et al. (2016).

41 resistivity of the first deeper body ("C2" in Fig. 1c) can be explained by the
42 presence of andesite melts in APMB (with a melt fraction $\phi_f > 0.15$), the
43 resistivity of the region above it ("C3" in Fig. 1c) may reflect the presence of
44 dacite melts combined with aqueous fluids (Comeau et al., 2016). A similar
45 vertically elongated structure is revealed also by the inversion of Bouguer
46 anomaly data that highlights a low density and ~ 15 -km-wide structure on
47 the top of the APMB (del Potro et al., 2013), interpreted as an active diapiric
48 ascent of magma (e.g. del Potro et al., 2013; Fialko and Pearse, 2012; Gotts-
49 mann et al., 2017). The presence of a mid-crustal diapir which slowly moves
50 upward is in agreement with geodesy data collected above APMB from 1995
51 to 2010 (Fialko and Pearse, 2012). InSAR data show indeed a ~ 150 -km-wide
52 region, centered on the western slope of Uturuncu volcano, which is uplifted
53 at the rate of ~ 1 cm/yr, and surrounded by an approximately 30-km-wide
54 ring of subsidence (Fig. 1a-b). The morphology and large extent of such a
55 "sombbrero"-shaped deformation on the surface cannot be caused by a single
56 large dike as expected for an intrusion in a merely elastic crust (Menand and
57 Tait, 2001; Jellinek and DePaolo, 2003). But instead it matches well results
58 of geodynamics models that assume the rise of a large diapir fed by partial
59 melt from the APMB within a crust that is not-purely elastic (e.g. Fialko and
60 Pearse, 2012; Gottsmann et al., 2017). Such a large diapir rising from the top
61 of APMB would cause an extensive deformation of the whole crust, leading
62 in turn to the displacement measured at the surface by geodesy techniques.

63 The interaction of the rising diapir with the crustal layer above offers
64 the opportunity to estimate the effective rheology of the crust itself. The
65 structure of the crust with its rheological properties and mechanical behavior

66 are indeed heavily influenced by the specific geodynamic context in which
67 the crust is located (Burov, 2011). So the rheology can in fact deviate from
68 the classical case where the whole deformation can be simply described by
69 a purely elastic or a purely viscous model. Moreover, heterogeneities that
70 characterize the crust on all scales, i.e. from small-scale (e.g. grain size, pore
71 fluid pressure, chemical activities of mineral components, etc.) to large-scale
72 (dikes filled with magma, faults, etc.), result in an intricate structure that
73 can easily be locked or "jammed". Thus at the macroscopic scale, the crust
74 bulk behavior could be comparable to that of a yield-stress material whereby
75 flow can only occur when a threshold stress value (i.e. the yield stress, σ_y)
76 is reached (Ancey, 2007; Bonn et al., 2017). Within this perspective, for an
77 heterogeneous lower-middle crust an effective viscoplastic rheology can be
78 claimed, making the yield stress a key aspect to better understand its bulk
79 behavior.

80 In this paper we infer the rheological properties of the lower-middle crust
81 below APVC from the rate of vertical surface displacement measured in the
82 orogenic region of the Altiplano and by assuming that this uplift is caused
83 by the rise of a diapir from above APMB. To do so we assume that the
84 heterogeneous crust surrounding the diapir behaves as a non-Newtonian yield
85 stress fluid, i.e. as a material whose bulk behavior can be described with a
86 viscoplastic rheological model. In section 2 we introduce the main rheological
87 properties of these materials. In section 3 we discuss the general critical
88 conditions for motion of a buoyant body through an yield stress fluid. The
89 latter are applied to the APMB case in section 4. We end by discussing the
90 implications that our results have for a partially molten lower-middle crust.

91 2. The yield-stress in viscoplastic rheology

92 Viscoplastic fluids (synonym of yield stress fluids) are characterized by
93 the presence of a yield stress, σ_y (Dinkgreve et al., 2017). A typical example
94 of them is a suspension of particles in a liquid. When the particle volume
95 fraction increases, the particles come into close contact, and the material
96 can face jamming. In this jammed state, the material can support stresses
97 without flowing. A so-called yield stress fluid does not flow unless the applied
98 stresses are large enough to unjam the structure, but it does flow when
99 the stresses become larger than σ_y . This introduces a non-linearity to the
100 material rheology, with strong impact on its dynamics (Makse et al., 2005;
101 Coussot, 2005; Barnes, 1995).

102 Simple yield stress fluids are those described by popular rheological mod-
103 els such as the Bingham model or the Hershel-Bulkley (HB) model. The
104 latter writes

$$\begin{aligned} \sigma &= \sigma_y + K_v \dot{\gamma}^n & \text{for } \sigma > \sigma_y & \quad (1) \\ \dot{\gamma} &= 0 & \text{for } \sigma \leq \sigma_y & \end{aligned}$$

105 where σ is the stress, $\dot{\gamma}$ the strain rate, K_v the consistency and n the
106 power-law exponent. Note that the exponent n defined here is the reverse
107 of the power law index usually used in equations for creep mechanisms in
108 geophysics (e.g. in Ranalli, 1995). For $n < 1$ the fluid is shear thinning and
109 the effective viscosity $\eta_{eff} = \sigma/\dot{\gamma}$ decreases as $\dot{\gamma}$ increases. For $n > 1$ the
110 fluid is shear thickening. For $n=1$ and $\sigma_y > 0$ the HB model reduces to the

111 Bingham model and describes a fluid with a linear flow curve and constant
112 value of viscosity. And, finally, for $n=1$ and $\sigma_y=0$ the fluid is Newtonian.

113 The concepts of yield stress and plasticity are not only employed in the
114 rheology of viscoplastic fluids, but they are also largely used in solid mechan-
115 ics through the Coulomb plasticity theory. In Coulomb plasticity, plastic
116 deformation indicates the irreversible deformation of a sample under stress
117 whereas in Bingham viscoplasticity it refers to a solid-liquid transition. In
118 this latter case the yield stress becomes the limit between the elastic (or
119 viscoelastic) solid-like domain and the viscous fluid-like domain where the
120 material flows. Even though the definition of σ_y is not the same among the
121 two theories, the concept behind it relies to some overlapping phenomena:
122 the transition from a reversible to a non-reversible deformation on one side
123 and the not-flowing to flowing on the other side. Besides that, however, the
124 two theories show some differences on their theoretical formulation (Ancy, 2007).
125 The main one regards the description of material's deformation on a
126 macroscopic scale: a viscoplastic fluid behaves as a whole on the bulk scale,
127 i.e. as a one-phase homogeneous material (Coussot et al., 2009). Hence, it
128 only requires a single stress-strain constitutive equation, e.g. eq.(1), where
129 there is no need to separate the role of interstitial fluids from the one of
130 the solid phase. This strongly differs from a two-phases saturated Coulomb
131 material in which the two phases can move at different velocities and have
132 to be considered separately.

133 Throughout the rest of this article, we will always refer for the fluid
134 deformation to the rheological viscoplastic description. That is describing
135 both mush and hot crust as a single-phase incompressible fluid that behaves

136 as a viscous fluid once set in motion.

137 **3. Conditions for the ascent of a buoyant instability in a yield-** 138 **stress fluid**

139 When a yield stress fluid is heated the buoyancy stresses that originate
140 due to thermal expansion may not be large enough to exceed the fluid yield
141 stress. Motion is then prevented and the fluid remains at rest. On the other
142 hand, when local stresses are large enough, a thermal plume can develop
143 and rise within the fluid column. The plume dynamics has been investi-
144 gated experimentally for a simple yield stress fluid heated by a local heat
145 source by Davaille et al. (2013) (see Appendix A for details on experimen-
146 tal conditions). They found that the formation and subsequent growth of a
147 thermal instability can be described in three main stages: (1) a no-motion
148 phase where a hot pocket grows by thermal diffusion around the localized
149 heat source (Fig. 2a and Fig. 3). (2) A stage where slow creep takes place
150 within the growing hot pocket (Fig. 2b). This slow ascent can be observed
151 also in the spatio-temporal evolution shown in Fig. 3 where bright lines that
152 correspond to reflecting particles formed by Thermo-Liquid Crystals (TLCs)
153 are not longer horizontal but begin to move upward. This is because, starting
154 from this stage, the edge of the thermal pocket begins to empty slowly to
155 feed a creep confined around the heating element (Fig. 2c). However, during
156 this phase the fluid outside the hot pocket still remains unyielded. And (3)
157 the stage in which a hot finger rises upward (Fig. 4a). Here upwelling oc-
158 curs only within the thermal anomaly and shear is strongly localized along
159 plume boundaries (Fig. 4b). The fluid within the anomaly moves then as a

160 plug and the overall thermal shape looks more like a finger than the classical
161 mushroom shape expected for Newtonian fluids.

162 For small Reynolds numbers, the flow resulting from the rising of the
163 thermal instability can be parameterized by two key dimensionless numbers.
164 The first is the Yield number, Y , and the second is the Bingham number, Bi
165 (Davaille et al., 2013; Karimfazli et al., 2016; Massmeyer et al., 2013). For
166 simplicity here we use the inverse of the Yield number, $Y_{inv} = 1/Y$, which
167 represents the ratio between the buoyancy stress and the yield stress. It is
168 usually written as

$$Y_{inv} = \frac{g\Delta\rho D}{3\sigma_y}. \quad (2)$$

169 where g is the acceleration due to gravity and $\Delta\rho$ the density difference
170 between the hot body, described by a characteristic diameter D , and the
171 ambient fluid. Y_{inv} has been firstly employed to evaluate motion of a single
172 rigid sphere in Bingham fluid (Beris et al., 1985). In this case, the critical
173 value of the (inverse) Yield number, Y_{invC} , below which the sphere does not
174 move is $Y_{invC}=6.99$. It has been subsequently confirmed experimentally for
175 simple HB fluids (Tabuteau et al., 2007) and for more heterogeneous HB
176 fluids (Sgreva et al., 2020a). In the case of buoyant thermal instabilities
177 instead of spheres, one can consider the hot pocket forming around the heat-
178 ing source at stage (1) and (2) as a buoyant "entity" that tries to go up
179 because it is less dense but is kept anchored at the original position by the
180 fluid yield stress. Davaille et al. (2013) found that the thermal instability
181 will rise only if $Y_{inv} > Y_{invC} = 8.8 \pm 0.7$, a value close to but different from
182 the solid sphere case. This is expected given the different geometries and

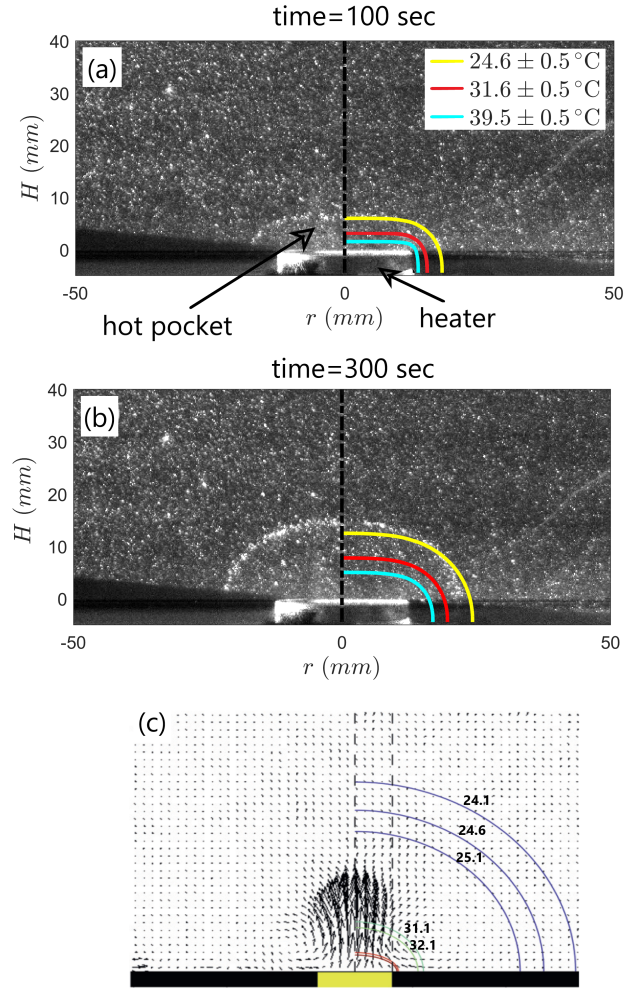


Figure 2: Front view of the growth of a hot pocket in a simple Herschel-Bulkley (HB) fluid (Carbopol) when heated from a localized heating source. Experiment from Davaille et al. (2013), see Appendix A for details on experimental conditions. In (a) and (b) the brighter lines are thermochromic liquid crystals' isotherms. The same isotherms are reproduced numerically in the conductive regime and plotted with different colors: yellow (24.6 ± 0.5 °C), red (31.6 ± 0.5 °C) and blue (39.5 ± 0.5 °C). Time is measured from the start of heating. (a) Growth of a hot pocket. Numerical isotherms fit well the experimental ones (stage (1) in the text). (b) Slow creep stage where the difference between experimental and numerical isotherms indicates the departure from the fully conductive regime (stage (2)). (c) Example of velocity field obtained during the slow creep stage. Solid lines indicate analytical isotherms for a steady-state conductive regime (values are indicated in °C). Significant vertical velocities are recorded at the center of the hot pocket and near the heater while outside the hot pocket the fluid remains motionless.

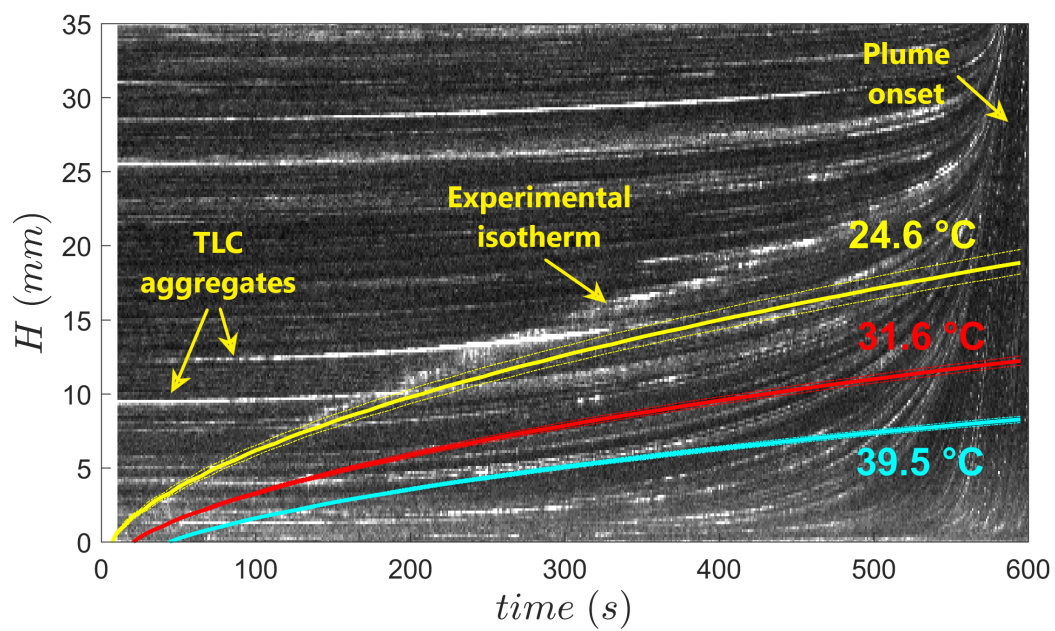


Figure 3: Spatiotemporal evolution of the experiment shown in Fig. 2. The figure shows the light intensity of the pixel line in the center of the setup as a function of time. Colored lines refer to the computed isotherms described in Fig. 2.

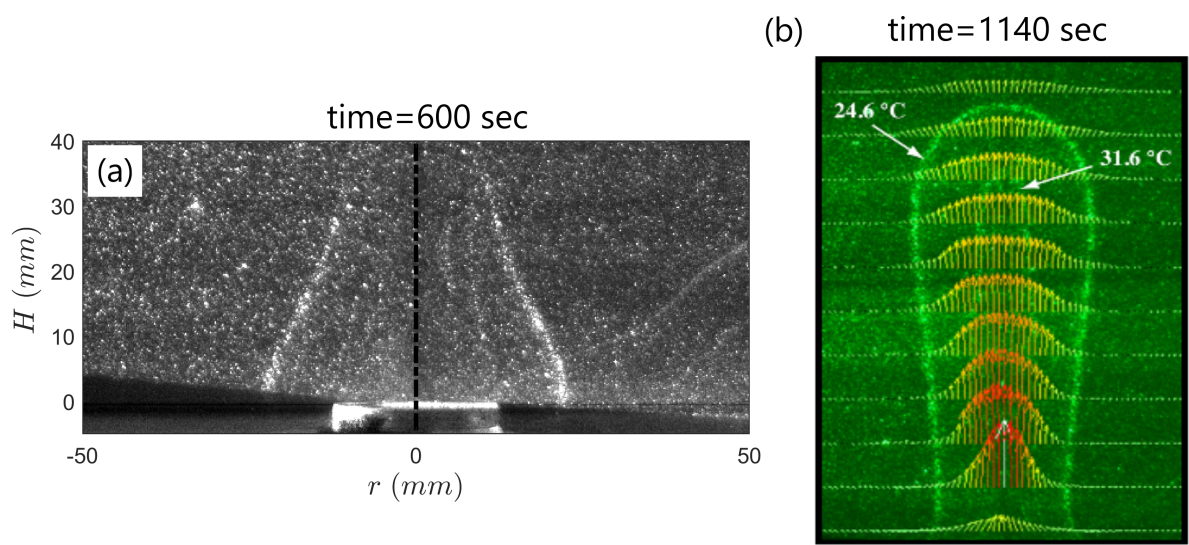


Figure 4: Last stage of the experiment shown in Fig. 2. (a) Rising of the hot plume, corresponding to stage (3) in the text. (b) Developed plume. Bright lines are isotherms. Colored vectors show the velocity field. Adapted from Davaille et al. (2013).

183 boundaries conditions, i.e. a bottom rigid boundary condition and a fluid-
184 fluid interface between hot pocket and ambient fluid in plume experiments,
185 and a bottom free surface boundary condition and a solid-fluid interface in
186 the experiments for the falling sphere. Y_{inv_C} has been afterwards evaluated
187 also from numerical simulations which investigate the development of ther-
188 mal plumes in a locally heated simple yield stress fluid (Massmeyer et al.,
189 2013; Sgreva, 2020b). For conditions similar to the experiments of Davaille
190 et al. (2013), namely a comparable fluid rheology, geometry of the setup
191 and imposed heating rate, they led to $Y_{inv_C} = 5.0 \pm 1.2$ in Massmeyer et al.
192 (2013) and 7.35 ± 0.35 in Sgreva (2020b) (Fig. 5). Differences in this case
193 can be related to the formulation of the numerical model, i.e. whether elas-
194 tic deformation in addition to viscoplasticity is used (Sgreva, 2020b) or not
195 (Massmeyer et al., 2013).

196 For a more geological perspective, the Yield number has already been
197 used, for instance, to describe the difficulties for magma transport in a dyke
198 through fracturing lithospheric rocks due to buoyancy forces (Weinberg and
199 Podladchikov, 1994). Although the formulation of Y_{inv} in this last case re-
200 mains the same as ours, by the definition of yield stress, Y_{inv} can evaluate a
201 different physical phenomena. For example, in Weinberg and Podladchikov
202 (1994) the yield stress used to calculate the Yield number is the rock's brittle
203 strength defined following Byerlee's law. The result for transporting magma
204 through dikes is that the condition of $Y_{inv} > Y_{inv_C}$ is very difficult to achieve
205 and to maintain without invoking other quite specific conditions, i.e. very
206 large magma bodies, proximity to the surface, tensile tectonics, etc.

207 Beside Y , diapir development also requires the Bingham number, Bi ,

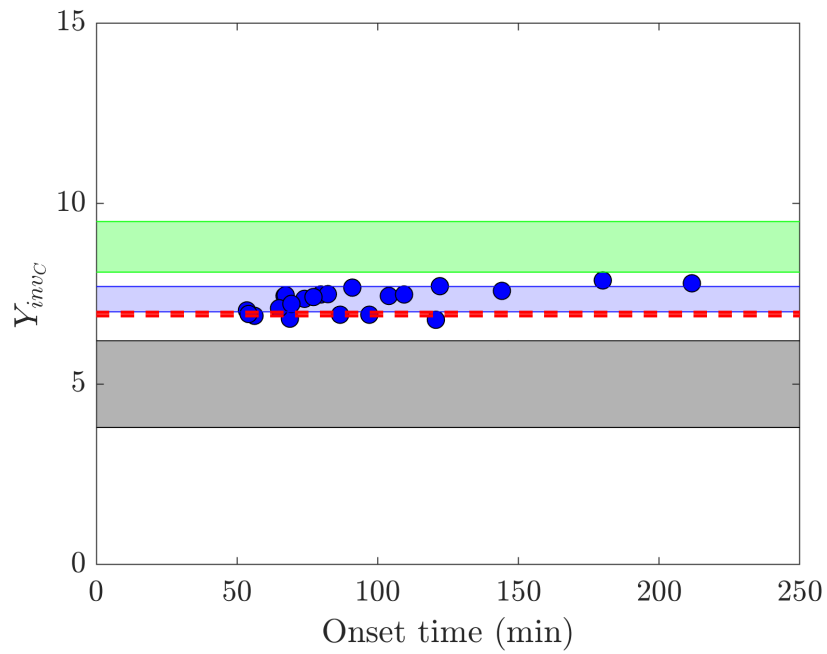


Figure 5: Inverse of the Yield number at the onset (Y_{inv_C}). Blue dots are simulations from Sgreva (2020b) and the blue bar corresponds to $Y_{inv_C} = 7.35 \pm 0.35$. Green bar indicates $Y_{inv_C} = 8.8 \pm 0.7$ (Davaille et al., 2013), gray bar $Y_{inv_C} = 5.0 \pm 1.2$ (Massmeyer et al., 2013) and red dashed line $Y_{inv_C} = 6.99$ (Beris et al., 1985; Tabuteau et al., 2007).

208 being supercritical, i.e. $Bi \leq 1$ (Massmeyer et al., 2013). The Bingham
 209 number compares the yield stress to the viscous stress and for a Herschel-
 210 Bulkley fluid writes:

$$Bi = \frac{\sigma_y}{K_v \dot{\gamma}^n}. \quad (3)$$

211 Motion is therefore expected only when local shear rates are larger than
 212 the critical strain rate corresponding to $Bi=1$, that is for $\dot{\gamma} > \dot{\gamma}_c = (\sigma_y/K_v)^{1/n}$
 213 (Fig. 6). It is only when the shear rate reaches this threshold that the hot
 214 pocket that grows from the hypothetical heating point evolves into a diapir.
 215 Note that when $Bi = 1$, the stress defined in eq. (1) is $\sigma_c = \sigma_y + K_v \dot{\gamma}_c^n = 2\sigma_y$
 216 and the effective critical viscosity writes:

$$\eta_c = \frac{\sigma_c}{\dot{\gamma}_c} = \frac{2\sigma_y}{(\sigma_y/K_v)^{1/n}}. \quad (4)$$

217 After the onset, the Bingham number decreases toward a value smaller
 218 than one (i.e. $Bi < 1$). For instance, in Sgreva (2020b) and Massmeyer et al.
 219 (2013) Bi was found to decrease up to 3 times from the value at the onset
 220 when the vertical velocity reaches its maximum (Fig. 6c). This decrease of
 221 Bi and the related increase in strain rate (i.e. $\dot{\gamma}/\dot{\gamma}_c > 1$) translates also into
 222 smaller effective viscosity. Hence the effective viscosity inferred at the onset
 223 ($\eta_{eff} = \eta_c$) represents the largest value of viscosity at which the transition
 224 from jamming to motion takes place and it will then decrease ($\eta_{eff} < \eta_c$)
 225 during the ascent of the diapir.

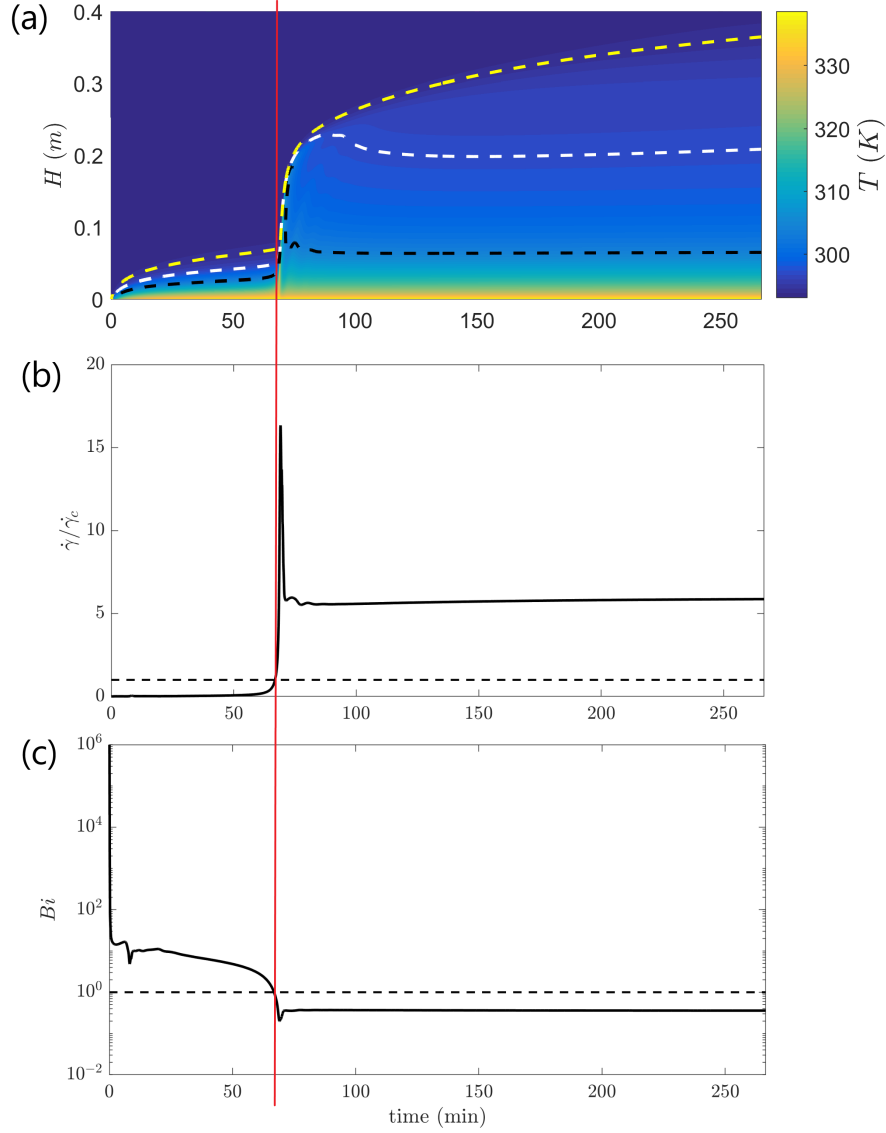


Figure 6: Development of a plume in a HB fluid, from simulation of Sgreva (2020b) ($\Delta T = 44$ °C; $\sigma_y = 0.076$ Pa; $Y_{invC} = 7.44$; $Ra \sim 10^5$). (a) Temporal evolution of temperature T along the central axis. Three isotherms have been highlighted: 21.0 °C (in yellow), 23.9 °C (in white) and 31.1 °C (in black). (b) Evolution of the strain rate $\dot{\gamma}$ normalized by the critical strain rate $\dot{\gamma}_c$ during the development and the rise of the hot instability. The critical strain rate is defined for $Bi = \sigma_y / (K_v \dot{\gamma}_c^n) = 1$. Dashed line indicated $\dot{\gamma}/\dot{\gamma}_c=1$. (c) Evolution of Bingham number. Dashed line indicated $Bi=1$. The vertical red line indicates when the Bingham number in (c) becomes one.

226 4. Constraints on the diapirism at APMB and crust's rheology

227 An active and rising diapir has been suggested as the cause of the up-
228 lift observed above the Altiplano-Puna Magma Body (Fialko and Pearse,
229 2012; Comeau et al., 2015). Geodesy data and leveling data show in fact a
230 continuous (since 1960s), nearly constant and slow uplifting of an about 100-
231 km-wide region of the Altiplano-Puna volcanic complex (Fialko and Pearse,
232 2012; Henderson and Pritchard, 2013; del Potro et al., 2013). The central
233 area which is being uplifted at about 1 cm/yr is also surrounded by a broad
234 ring of subsidence forming a global sombrero-shape uplift which is consistent
235 with the presence of a diapir deep inside the crust. In this case the diapir
236 would develop from the APMB within a framework of a heterogeneous crust
237 and at greater depth than the brittle-ductile transition. The latter is reported
238 between 4.5 and 10 km below the Altiplano (Jay et al., 2012) whereas the
239 APMB extends from a depth of ~ 20 km below the surface (Comeau et al.,
240 2015).

241 In the previous section we have shown how that two main conditions
242 must be satisfied to allow the ascent of a buoyant instability in a yield stress
243 medium. The first one regards the inverse of the Yield number (here we
244 consider $Y_{inv} > Y_{inv_C} = 7.35 \pm 0.35$ from Sgreva (2020b)), while the second
245 one is accounted by $Bi \leq 1$. Given these two conditions, one can evaluate
246 the emplacement conditions for a buoyant instability (e.g. a diapir) in a
247 jammed crustal mush with HB rheology. We do so for the case of APMB,
248 assuming that the uplift measured at the surface originates from the rising
249 of a hot diapir from the shallowest regions of the magmatic reservoir beneath
250 Ulturuncu volcano and rises with a vertical velocity equal to what is measured

251 at the surface, i.e. $v_z=1$ cm/yr (Fialko and Pearse, 2012).

252 In Fig. 7, we show conditions which lead to $Y_{inv} = Y_{inv_C}$ for such a sys-
253 tem. According to geodesy data (Fialko and Pearse, 2012; Gottsmann et al.,
254 2017) and magnetotellurics (Comeau et al., 2016), we assume a characteris-
255 tic diameter $D_{diap}=10-100$ km for the diapir. The density contrast between
256 diapir and surrounding crust is not well constrained and varies between dif-
257 ferent models. Fialko and Pearse (2012) use in their numerical simulations a
258 density difference of $\Delta\rho=400$ kg/m³, whereas smaller values of ~ 100 kg/m³
259 are employed for example by Gottsmann et al. (2017) and Spang et al. (2019).
260 A similar range of possible $\Delta\rho$, based on the inversion of gravity anomalies,
261 is given by del Potro et al. (2013). An upper limit for the density contrast of
262 400 kg/m³ represents an enormous density anomaly produced by the melt-
263 ing of a large enough amount of material below the observed diapiric body.
264 Given a crust density of $\rho_c=2700$ kg/m³, this scenario would require, for in-
265 stance, the presence of a very large melt fraction (ϕ_f), that is $\phi_f \sim 0.9$ for a
266 dacitic melt with $\rho_d=2300$ kg/m³ (del Potro et al., 2013). On the other hand,
267 an overall smaller density contrast reflects a smaller melt fraction which can
268 decrease towards the limit of $\Delta\rho=50$ kg/m³ for a fully crystallized dacite
269 ($\phi_f=0$; $\rho_d=2650$ kg/m³).

270 Within these ranges of diapir's size and density contrast, we find that
271 a diapir can rise and deform the surrounding crust if the latter has a yield
272 stress within a range of 0.5 and 15 MPa (Fig. 7). Larger values of yield
273 stress clearly need either a broader instability or an unlikely larger density
274 contrast. Here the yield stress has to be interpreted within the rheological
275 definition, i.e. as the stress value needed to unjam a locked medium and to

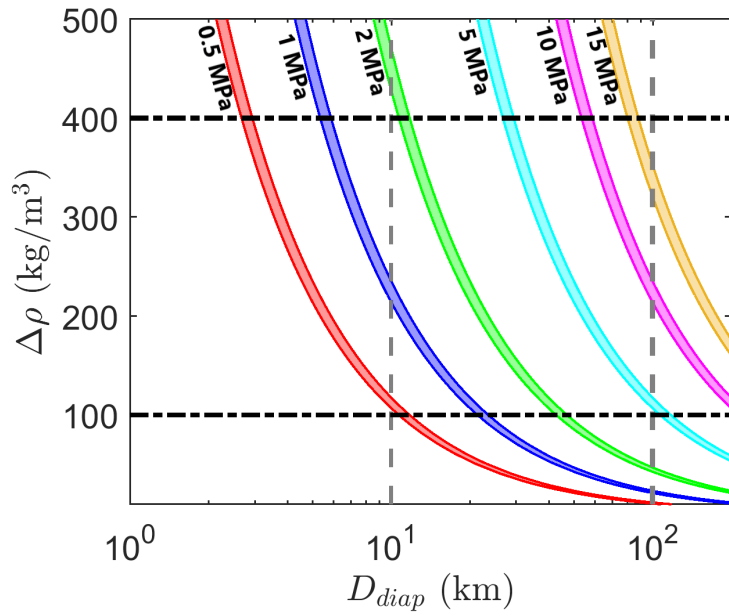


Figure 7: Yield stress (colored lines) allowing the development of a diapir from the top of the APMB according to $Y_{invC} = 7.35 \pm 0.35$, as function of diapir diameter and density contrast.

276 allow it to flow, rather than the threshold at which the medium simply loses
 277 the reversibility in deformation.

278 Beside $Y_{inv} > Y_{invC}$, the other condition for motion is $Bi \leq 1$. As summa-
 279 rized above, this critical condition translates into a critical minimum strain
 280 rate required for motion $\dot{\gamma}_c = (\sigma_y/K_v)^{(1/n)}$ and an effective viscosity is then
 281 given by $\eta_c = 2\sigma_y/\dot{\gamma}_c$ (eq. (4)). In Fig. 8 we display this viscosity as a
 282 function of fluid consistency and the range of yield stress found previously
 283 (i.e. σ_y in between 0.5 and 15 MPa). We take two limit values for the shear
 284 thinning index, namely $n=0.25$ (Fig. 8a) and $n=0.5$ (Fig. 8b). They cor-
 285 respond to stress exponents $n_E=1/n$ in stress-strain relationships for creep
 286 of 4 and 2, respectively, as expected for rocks Ranalli (1995). The viscosity
 287 reported in Fig. 8 corresponds to the maximum effective viscosity calculated
 288 from the minimum strain rate that guarantees $Bi=1$. As expected from its
 289 definition, it depends on the value of fluid consistency that one uses in the
 290 HB model. A way to bound the consistency is by taking into account the
 291 maximum vertical velocity, v_{max} , at which the thermal instability is moving
 292 upward. From the condition $Bi \leq 1$, one can in fact relate v_{max} to the size of
 293 the instability and the critical strain rate:

$$v_{max} = C2r_{eq}\dot{\gamma}_c, \quad (5)$$

294 where C is an experimental constant. Based on numerical simulations (Sgreva,
 295 2020b), the maximum velocity is found to scale as $v_{max} \sim 4.45(2r_{eq}\dot{\gamma}_c)$ for
 296 constant $n=0.58$ (Fig. 9). The simulations of Massmeyer et al. (2013) where
 297 n was varied between 0.50 and 0.90 present the same trend (Fig. 9). The
 298 small differences between the two studies for same n displayed in Fig. 9 can be

299 related to the different formulation of the numerical model used to simulate
 300 plume’s formation, namely a regularized viscoplastic model in Massmeyer
 301 et al. (2013) and an elasto-viscoplastic model in Sgreva (2020b).

302 Considering the recorded uplift velocity at the surface v_z as a possible
 303 maximum rising velocity of the diapir, for the case at APMB the scaling of
 304 v_{max} translates to

$$v_z \sim 4.45 D_{diap} \dot{\gamma}_c, \quad (6)$$

305 leading to a critical strain rate of $\dot{\gamma}_c = v_z / (4.45 D_{diap})$. Within the chosen
 306 interval of D_{diap} , the critical strain rate is $\sim 10^{-15} - 10^{-16} \text{ s}^{-1}$. The resulting
 307 consistency is therefore

$$K_v = \sigma_y \dot{\gamma}_c^{-n} = \sigma_y \left(\frac{4.45 D_{diap}}{v_z} \right)^n. \quad (7)$$

308 This value of K_v is reported in Fig. 8 for the interval of diapir’s sizes of
 309 10-100 km.

310 5. Discussion

311 Given the evidence of partial melt and the shallow ductile-brittle tran-
 312 sition, a simple elastic model for the lower-middle crust beneath APVC is
 313 not appropriate to properly describe the whole system but instead a more
 314 complicated rheological model is required. The HB framework developed in
 315 the previous sections provides estimates of the lower-middle crust effective
 316 yield stress and viscosity at APMB.

317 The first crucial aspect regards the proper definition of yield stress needed
 318 to evaluate the conditions of motion. Differently from the already mentioned

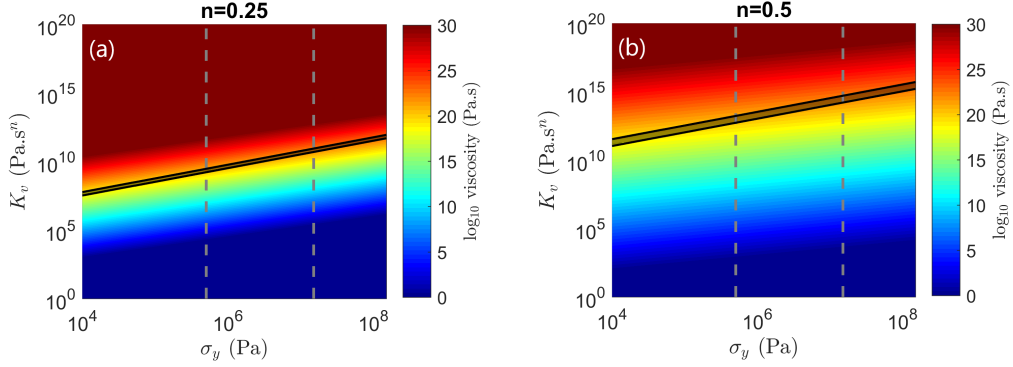


Figure 8: Maximum value of critical effective viscosity η_c (eq.4) corresponding to $Bi=1$, as function of consistency K_v and yield stress σ_y . Grey dashed lines bound the range of yield stress after Fig. 7. Black bands indicate $K_v = \sigma_y (4.45 D_{diap}/v_z)^n$, with D_{diap} between 10 and 100 km and an uplift velocity of $v_z=1$ cm/yr (Fialko and Pearse, 2012). (a) Shear thinning exponent $n=0.25$ and (b) $n=0.5$.

319 work of Weinberg and Podladchikov (1994), in our equation of the Yield
 320 number, σ_y does not indicate the stress threshold needed to the brittle failure
 321 of the rocks in the crust but it instead represents the threshold to unjam the
 322 locked medium, which could for example involve reactivation of fractures and
 323 creep. When Y_{inv} is defined to evaluate the ability of the system to transport
 324 magma by opening new fractures it must involve yield strength for ambient
 325 rocks in the order of 10^2 - 10^3 MPa, making it dramatically difficult to achieve
 326 conditions of $Y_{inv} > Y_{invC}$. However, the rheological (jamming) transition
 327 in partially molten rocks that takes place when the solid-particles volume
 328 fraction (ϕ_s) decreases approaching the maximum packing fraction ($\phi_m \sim 0.6$)
 329 can lead to a strength drop which can span up to four orders of magnitude
 330 (Rosenberg and Handy, 2005; Cashman et al., 2017). In addition to this
 331 strong dependence on ϕ_s and hence on the melt fraction ϕ_f , the measurement

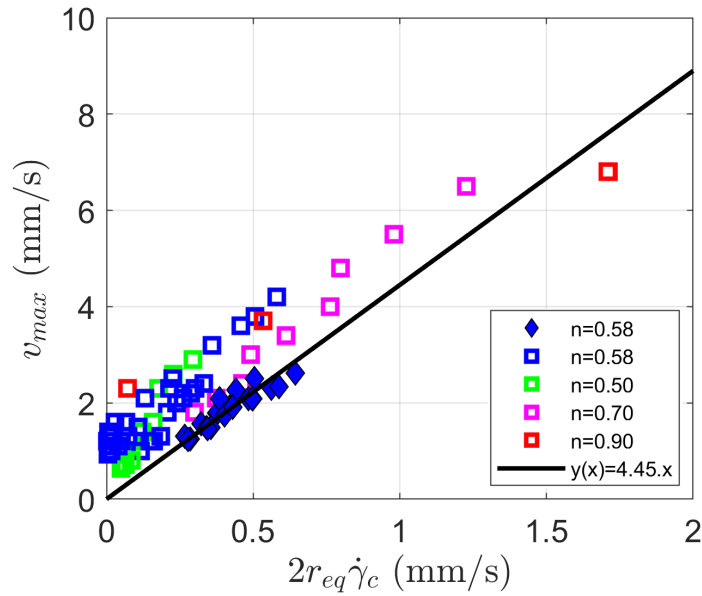


Figure 9: Maximum rising velocity of an hot instability as a function of the product between equivalent diameter $D_{eq} = 2r_{eq}$ and critical strain rate. Diamond symbols refer to numerical simulations of thermal plumes in a yield stress fluid of Sgreva (2020b) computed with a power-law index $n = 0.58$. The later are fitted by the equation $y(x) = 4.45x$. Squared symbols refer to simulations of Massmeyer et al. (2013) and colors are for the different power-index n tested.

332 of the strength of a partially molten rock with relative large melt fraction
 333 (≥ 0.3) falls also very close to the minimum measurable value of σ_y from
 334 experimental apparatus. The latter is estimated around ~ 1 MPa (Pistone
 335 et al., 2012; Rosenberg and Handy, 2005; Caricchi et al., 2007). In this
 336 regard, the range of σ_y of 0.5-15 MPa we found in Fig. 7 for the hot ductile
 337 crust that surrounds the rising diapir corresponds, in order of magnitude,
 338 to the strength of partially molten granite with $\phi_f \sim 0.25$ in Rosenberg and
 339 Handy (2005) (where $\sigma_y \sim 1$ MPa) and those for crustal granitic rocks on the
 340 western Arabian Peninsula, where $\sigma_y \sim 1-3$ MPa (Jónsson, 2012).

341 The second aspect that arises from the ascent of a diapir at APMB regards
 342 the values of effective viscosity and strain rate we have found. According to
 343 Fig. 7, a diapir of $D_{diap}=50$ km and $\Delta\rho=100$ kg/m³ would set on motion and
 344 would travel through a crust with yield stress of around $\sigma_y=2.2$ MPa. By tak-
 345 ing the typical stress exponent expected for creep mechanisms of lower-middle
 346 crustal rocks, that is $n_E=n^{-1}=3.0$ (Ranalli, 1997), the previous conditions
 347 lead to a consistency of $\sim 10^{13}$ Pa s^{0.3} and to an effective maximum value
 348 of viscosity for the lower-middle crust above APMB of $\eta_c \sim 10^{21}$ Pa s. This
 349 value corresponds to what is needed to trigger the rise of the diapir since it
 350 is calculated from the critical condition of $Bi=1$. However, after the plume
 351 onset, Bi continues to decrease (Fig. 6c) while the strain rate increases (Fig.
 352 6b), leading in turn to values of effective viscosity that are lower than those
 353 found for $Bi=1$. From eq. (6), considering a vertical velocity of 1 cm/yr, the
 354 critical strain rate results in $\dot{\gamma}_c \sim 10^{-15}$ s⁻¹ for a 50-km-wide diapir. Hence,
 355 at conditions of $Bi < 1$ where the strain rate can increase up to one order of
 356 magnitude compared with $\dot{\gamma}_c$ (Fig. 6b), we can expect a crustal region that

357 deforms at a strain rate of 10^{-14} s^{-1} . This corresponds to values of strain
358 rate previously employed for APVC, e.g. $\sim 10^{-14} \text{ s}^{-1}$ in Jay et al. (2012),
359 and other compression areas, such as Southern-Tibet where $\dot{\gamma} \sim 10^{-14}$ - 10^{-15}
360 s^{-1} (Wang et al., 2019; Molnar, 2020) and Southern-Aegean where $\dot{\gamma} \sim 10^{-15}$
361 s^{-1} (Kreemer and Chamot-Rooke, 2004; Kumar and Gordon, 2009).

362 Regarding the critical effective viscosity value, we found $\eta_c \sim 10^{21} \text{ Pa s}$.
363 Such a high viscosity corresponds in order of magnitudes to the one of
364 hot sub-solidus host rocks inside which magma bodies are usually emplaced
365 (Sparks et al., 2019). To our knowledge, for the specific case at APMB there
366 are not many independent constraints on the viscosity of the lower-middle
367 crust. A list of them is reported in Table 1. The viscosity of the partially
368 molten zone has been inferred from resistivity maps by Comeau et al. (2016)
369 who estimated a viscosity of $\eta \sim 10^{12} - 10^{16} \text{ Pa s}$ with 20% melt fraction for
370 the shallow magma reservoir. Viscosity of around $\eta \sim 10^{16} - 10^{18} \text{ Pa s}$ has
371 been estimated by Fialko and Pearse (2012) by assuming a linear Maxwell
372 viscoelastic rheology for the lower-middle crust. Similar values ($< 10^{16} \text{ Pa s}$)
373 are obtained by using the same viscoelastic rheology for the structure be-
374 neath APVC also by Gottsmann et al. (2017). However, although those
375 values mainly represent either the viscosity of the APMB itself or that of
376 the hot diapir rising from it, they do not give much information about the
377 effective bulk viscosity of the whole inelastic crust. The latter should have
378 in fact a reasonable larger value of η due to the contribution of the regions
379 of the crust where both temperature and melt fraction are lower than the
380 APMB's. Rheological measurements on larger timescales (i.e. millions of
381 years) resulting from the analysis of lithosphere response to unloading of the

Table 1: Effective viscosities beneath APVC. "VE model" indicate simulations carried out with a viscoelastic (VE) rheology.

Technique	Viscosity (Pa s)	Reference
VE model	$\sim 10^{16} - 10^{18}$ for APMB	Fialko and Pearce (2012)
VE model	$< 10^{16}$ for APMB; $\sim 10^{16} - 10^{19}$ for diapir	Gottsmann et al. (2017)
VE model	$< 10^{21} - 10^{22}$ at ~ 20 km beneath APVC	Gerbault et al. (2005)
from resistivity model	$< 10^{16}$ for APMB with 20% melt	Comeau et al. (2016)
from paleo-lake load	$< 5 \times 10^{20}$ for crustal plate	Bills et al. (1994)

382 large paleo-lake in the Central Andes of Bills et al. (1994) give in fact a viscos-
383 ity for the crustal plate that is larger than what predicted for APMB alone.
384 The maximum effective bulk viscosity obtained in this way is $\eta < 5 \times 10^{20}$
385 Pa s, definitely closer to the estimation for the maximum critical viscosity η_c
386 we obtain by using a HB rheology (Fig. 8).

387 6. Conclusion

388 In this work we propose a mechanical interpretation for the well doc-
389 umented uplift above APMB, based on the assumption that the effective
390 rheology at large scale of the crust is the one of a yield stress material. In
391 material with such rheology, the diapir take-off and growth require two local
392 conditions: (1) the ratio between yield stress and viscous stress to be super-
393 critical ($Bi < 1$), and (2) the ratio between the buoyancy stress of the hot
394 diapir and the yield stress to be larger than a critical value ($Y_{inv} > Y_{invC}$).

395 We find that in order to allow the formation and the rise of a 10-100
396 km-wide diapir from above APMB with a density contrast with respect to

397 surrounding rocks of 100-400 kg/m³, the lower ductile crust needs a yield
 398 stress of ~0.5-15 MPa to respect condition (1). Moreover, from condition (2)
 399 with an uplift velocity of 1 cm/yr, we can bound the maximum bulk effective
 400 viscosity η_c for the APMB lower-middle crust at $\eta_c \sim 10^{21}$ Pa s.

401 **Appendix A. Details on experiments of thermal plumes**

402 Figures 2 - 4 show the experiments on the development of thermal plumes
 403 in Carbopol of Davaille et al. (2013). These experiments are carried out
 404 by using a 166-mm-high rectangular tank into which the fluid is poured.
 405 The fluid is heated by a circular heater located at the center of the bottom
 406 surface. The maximal imposed temperature difference between the heater
 407 and the ambient fluid is $\Delta T \sim 44$ °C. The fluid rheology is described with
 408 a HB model with the following parameters: $\sigma_y=0.10$ Pa, $n=0.54$, $K_v=0.76$
 409 Pa s^{*n*}. For the case in Figs. 2 - 4, the Rayleigh number at the onset of motion
 410 is

$$Ra = \frac{\alpha \rho g \Delta T h^3}{k \eta_c} \sim 10^6, \quad (\text{A.1})$$

411 with α being the fluid thermal expansion (4.62×10^{-4} K⁻¹), ρ the density
 412 (1142 kg/m³), k the thermal diffusivity (1×10^{-7} m²/s), η_c the viscosity ob-
 413 tained from eq. (4) and h the height of the tank. The critical Yield number
 414 found in Davaille et al. (2013) ($Y_{invC} = 8.8 \pm 0.7$) can be determined from eq.
 415 (2) during stages (1) and (2) of plume development by assuming $D=2r_{eq}$,
 416 with r_{eq} being the equivalent radius of a sphere having the same volume as
 417 the hot pocket. Experimentally, the hot pocket can be quantitatively de-
 418 fined within the temperature field by the isotherm $T_{lim} = 0.1 \Delta T$, where

419 $\Delta T = T_{max} - T_{amb}$ and T_{max} is the heater temperature and T_{amb} the ambient
420 temperature. The hot pocket is therefore represented by the volume of fluid
421 with $T \geq T_{lim}$. For the density difference term in eq. (2) one can refer to the
422 mean $\Delta\rho$ within the fluid pocket, that is $\Delta\rho \simeq \overline{\Delta\rho} = \alpha\rho(\overline{T}_{hot\ pocket} - T_{amb})$
423 where $\overline{T}_{hot\ pocket}$ is the average temperature of the pocket.

424 **Acknowledgments**

425 N.R. Sgreva was supported by the Initial Training Network No. 642029-
426 ITN CREEP, an Horizon 2020 - Marie Skłodowska-Curie Action. This re-
427 search was also supported by LabEx PALM (ANR-10-LABX-0039- PALM).

428 **Data Availability**

429 The data underlying this article will be shared on reasonable request to
430 the corresponding author.

431 **References**

- 432 Ancey, C., 2007. Plasticity and geophysical flows: a review. *Journal of*
433 *Non-Newtonian Fluid Mechanics* 142, 4–35.
- 434 Barnes, H.A., 1995. A review of the slip (wall depletion) of polymer solutions,
435 emulsions and particle suspensions in viscometers: its cause, character, and
436 cure. *Journal of Non-Newtonian Fluid Mechanics* 56, 221–251.
- 437 Beris, A., Tsamopoulos, J., Armstrong, R., Brown, R., 1985. Creeping mo-
438 tion of a sphere through a Bingham plastic. *Journal of Fluid Mechanics*
439 158, 219–244.
- 440 Bills, B.G., De Silva, S.L., Currey, D.R., Emenger, R.S., Lillquist, K.D.,
441 Donnellan, A., Worden, B., 1994. Hydro-isostatic deflection and tectonic
442 tilting in the central Andes: Initial results of a gps survey of lake minchin
443 shorelines. *Geophysical Research Letters* 21, 293–296.

- 444 Bonn, D., Denn, M.M., Berthier, L., Divoux, T., Manneville, S., 2017. Yield
445 stress materials in soft condensed matter. *Reviews of Modern Physics* 89,
446 035005.
- 447 Burov, E.B., 2011. Rheology and strength of the lithosphere. *Marine and*
448 *Petroleum Geology* 28, 1402–1443.
- 449 Caricchi, L., Burlini, L., Ulmer, P., Gerya, T., Vassalli, M., Papale, P., 2007.
450 Non-newtonian rheology of crystal-bearing magmas and implications for
451 magma ascent dynamics. *Earth and Planetary Science Letters* 264, 402–
452 419.
- 453 Cashman, K.V., Sparks, R.S.J., Blundy, J.D., 2017. Vertically extensive and
454 unstable magmatic systems: a unified view of igneous processes. *Science*
455 355, eaag3055.
- 456 Chmielowski, J., Zandt, G., Haberland, C., 1999. The central Andean
457 Altiplano-Puna magma body. *Geophysical Research Letters* 26, 783–786.
- 458 Comeau, M.J., Unsworth, M.J., Cordell, D., 2016. New constraints on the
459 magma distribution and composition beneath Volcán Uturuncu and the
460 southern Bolivian Altiplano from magnetotelluric data. *Geosphere* 12,
461 1391–1421.
- 462 Comeau, M.J., Unsworth, M.J., Ticona, F., Sunagua, M., 2015. Magnetotel-
463 luric images of magma distribution beneath Volcán Uturuncu, Bolivia:
464 Implications for magma dynamics. *Geology* 43, 243–246.
- 465 Coussot, P., 2005. Rheometry of pastes, suspensions, and granular materials:
466 applications in industry and environment. John Wiley & Sons.

- 467 Coussot, P., Tocquer, L., Lanos, C., Ovarlez, G., 2009. Macroscopic vs. local
468 rheology of yield stress fluids. *Journal of Non-Newtonian Fluid Mechanics*
469 158, 85–90.
- 470 Davaille, A., Gueslin, B., Massmeyer, A., Di Giuseppe, E., 2013. Thermal
471 instabilities in a yield stress fluid: existence and morphology. *Journal of*
472 *Non-Newtonian Fluid Mechanics* 193, 144–153.
- 473 Dinkgreve, M., Denn, M.M., Bonn, D., 2017. Everything flows?: Elastic
474 effects on startup flows of yield-stress fluids. *Rheologica Acta* 56, 189–194.
- 475 Fialko, Y., Pearse, J., 2012. Sombrero uplift above the Altiplano-Puna
476 magma body: Evidence of a ballooning mid-crustal diapir. *Science* 338,
477 250–252.
- 478 Gerbault, M., Martinod, J., Hérail, G., 2005. Possible orogeny-parallel lower
479 crustal flow and thickening in the Central Andes. *Tectonophysics* 399,
480 59–72.
- 481 Gonnermann, H.M., Manga, M., 2007. The fluid mechanics inside a volcano.
482 *Annual Review of Fluid Mechanics* 39, 321–356.
- 483 Gottsmann, J., Blundy, J., Henderson, S., Pritchard, M., Sparks, R., 2017.
484 Thermomechanical modeling of the Altiplano-Puna deformation anomaly:
485 Multiparameter insights into magma mush reorganization. *Geosphere* 13,
486 1042–1065.
- 487 Henderson, S., Pritchard, M., 2013. Decadal volcanic deformation in the
488 Central Andes Volcanic Zone revealed by InSAR time series. *Geochemistry,*
489 *Geophysics, Geosystems* 14, 1358–1374.

- 490 Jay, J.A., Pritchard, M.E., West, M.E., Christensen, D., Haney, M., Minaya,
491 E., Sunagua, M., McNutt, S.R., Zabala, M., 2012. Shallow seismicity,
492 triggered seismicity, and ambient noise tomography at the long-dormant
493 Uturuncu Volcano, Bolivia. *Bulletin of Volcanology* 74, 817–837.
- 494 Jellinek, A.M., DePaolo, D.J., 2003. A model for the origin of large silicic
495 magma chambers: precursors of caldera-forming eruptions. *Bulletin of*
496 *Volcanology* 65, 363–381.
- 497 Jónsson, S., 2012. Tensile rock mass strength estimated using InSAR. *Geo-*
498 *physical Research Letters* 39.
- 499 Karimfazli, I., Frigaard, I., Wachs, A., 2016. Thermal plumes in viscoplastic
500 fluids: Flow onset and development. *Journal of Fluid Mechanics* 787, 474–
501 507.
- 502 Kreemer, C., Chamot-Rooke, N., 2004. Contemporary kinematics of the
503 southern aegean and the mediterranean ridge. *Geophysical Journal Inter-*
504 *national* 157, 1377–1392.
- 505 Kumar, R.R., Gordon, R.G., 2009. Horizontal thermal contraction of oceanic
506 lithosphere: The ultimate limit to the rigid plate approximation. *Journal*
507 *of Geophysical Research: Solid Earth* 114.
- 508 Makse, H.A., Brujic, J., Edwards, S.F., 2005. Statistical mechanics of
509 jammed matter (2005). arXiv preprint cond-mat/0503081 .
- 510 Massmeyer, A., Di Giuseppe, E., Davaille, A., Rolf, T., Tackley, P.J., 2013.
511 Numerical simulation of thermal plumes in a Herschel–Bulkley fluid. *Jour-*
512 *nal of Non-Newtonian Fluid Mechanics* 195, 32–45.

- 513 Massol, H., Jaupart, C., 2009. Dynamics of magma flow near the vent:
514 Implications for dome eruptions. *Earth and Planetary Science Letters*
515 279, 185 – 196.
- 516 Menand, T., Tait, S.R., 2001. A phenomenological model for precursor vol-
517 canic eruptions. *Nature* 411, 678–680.
- 518 Molnar, P., 2020. The brittle-plastic transition, earthquakes, temperatures,
519 and strain rates. *Journal of Geophysical Research: Solid Earth* 125,
520 e2019JB019335.
- 521 Pistone, M., Caricchi, L., Ulmer, P., Burlini, L., Ardia, P., Reusser, E.,
522 Marone, F., Arbaret, L., 2012. Deformation experiments of bubble-and
523 crystal-bearing magmas: Rheological and microstructural analysis. *Jour-
524 nal of Geophysical Research: Solid Earth* 117.
- 525 del Potro, R., Díez, M., Blundy, J., Camacho, A.G., Gottsmann, J., 2013. Di-
526 apiric ascent of silicic magma beneath the Bolivian Altiplano. *Geophysical
527 Research Letters* 40, 2044–2048.
- 528 Pritchard, M., De Silva, S., Michelfelder, G., Zandt, G., McNutt, S.R., Gotts-
529 mann, J., West, M., Blundy, J., Christensen, D., Finnegan, N., et al.,
530 2018. Synthesis: PLUTONS: Investigating the relationship between plu-
531 ton growth and volcanism in the Central Andes. *Geosphere* 14, 954–982.
- 532 Ranalli, G., 1995. *Rheology of the Earth*. Springer Science & Business Media.
- 533 Ranalli, G., 1997. Rheology and deep tectonics. *Annals of Geophysics* 40.

- 534 Rosenberg, C., Handy, M., 2005. Experimental deformation of partially
535 melted granite revisited: implications for the continental crust. *Journal of*
536 *metamorphic Geology* 23, 19–28.
- 537 Sgreva, N.R., 2020b. Influence of the fluid structure and elasticity on mo-
538 tions in a yield-stress material. Implications for geological systems. Theses.
539 Université Paris-Saclay. URL: <http://www.theses.fr/2020UPASJ002>.
- 540 Sgreva, N.R., Davaille, A., Kumagai, I., Kurita, K., 2020a. Interaction be-
541 tween a falling sphere and the structure of a non-newtonian yield-stress
542 fluid. *Journal of Non-Newtonian Fluid Mechanics* 284, 104355.
- 543 Spang, A., Baumann, T., Kaus, B.J., 2019. 3D geodynamic models of the
544 present-day Altiplano-Puna magmatic system. *AGUFM 2019*, V23H–0194.
- 545 Sparks, R., Annen, C., Blundy, J., Cashman, K., Rust, A., Jackson, M., 2019.
546 Formation and dynamics of magma reservoirs. *Philosophical Transactions*
547 *of the Royal Society A* 377, 20180019.
- 548 Tabuteau, H., Coussot, P., de Bruyn, J.R., 2007. Drag force on a sphere
549 in steady motion through a yield-stress fluid. *Journal of Rheology* 51,
550 125–137.
- 551 Turner, S., Costa, F., 2007. Measuring timescales of magmatic evolution.
552 *Elements* 3, 267–272.
- 553 Wang, H., Wright, T.J., Liu-Zeng, J., Peng, L., 2019. Strain rate distribution
554 in south-central Tibet from two decades of InSAR and GPS. *Geophysical*
555 *Research Letters* 46, 5170–5179.

- 556 Ward, K.M., Zandt, G., Beck, S.L., Christensen, D.H., McFarlin, H., 2014.
557 Seismic imaging of the magmatic underpinnings beneath the Altiplano-
558 Puna volcanic complex from the joint inversion of surface wave dispersion
559 and receiver functions. *Earth and Planetary Science Letters* 404, 43–53.
- 560 Weinberg, R.F., Podladchikov, Y., 1994. Diapiric ascent of magmas through
561 power law crust and mantle. *Journal of Geophysical Research: Solid Earth*
562 99, 9543–9559.
- 563 Zandt, G., Leidig, M., Chmielowski, J., Baumont, D., Yuan, X., 2003. Seis-
564 mic detection and characterization of the Altiplano-Puna magma body,
565 central Andes. *Pure and Applied Geophysics* 160, 789–807.